APPLIED SCIENCES AND ENGINEERING

# In situ stiffness manipulation using elegant curved origami

**Zirui Zhai[1], Yong Wang[2], Ken Lin[2], Lingling Wu[1], Hanqing Jiang[1]***



**The capability of stiffness manipulation for materials and structures is essential for tuning motion, saving energy, and delivering high power. However, high-efficiency in situ stiffness manipulation has not yet been successfully achieved despite many studies from different perspectives. Here, curved origami patterns were designed to accomplish in situ stiffness manipulation covering positive, zero, and negative stiffness by activating predefined creases on one curved origami pattern. This elegant design enables in situ stiffness switching in lightweight and space-saving applications, as demonstrated through three robotic-related components. Under a uniform load, the curved origami can provide universal gripping, controlled force transmissibility, and multistage stiffness response. This work illustrates an unexplored and unprecedented capability of curved origami, which opens new applications in robotics for this particular family of origami patterns.**

## INTRODUCTION

The stiffness of a material or a structure is of key importance in most, if not all, applications, with positive stiffness as a common property for bearing loads and transferring motion (*1*), zero (or quasi-zero) stiffness for vibration isolation and protection (*2*), negative stiffness for fast switching between states (*3*), high-speed actuation (*4*–*6*), and programmed deformation (*7*). Many species have ingenious mechanisms to switch among different stiffnesses to maintain motion, save energy, or deliver high power (*8*, *9*). Scientists and engineers have also deliberately created various means to manipulate stiffness for various applications, including in automotive (*10*), robotics (*11*), and aerospace components (*12*). However, these mechanisms are rather complicated (e.g., spring structures) and often require considerable energy inputs [e.g., electromagnetic and piezoelectric mechanisms (*6*, *13*)], which unfortunately cannot be used in size-limited applications [e.g., small robots (*14*), soft robots without rigid parts (*15*), or passive systems without power input (*16*)], although these applications may represent the true need for in situ stiffness manipulation. To somewhat circumvent the complex structures and expensive energy input, mechanical metamaterials have been designed to achieve stiffness manipulation using simple mechanisms (*17*–*20*); however, for a given metamaterial, the range of manipulation is limited and cannot switch all the way from positive to negative. Mechanical metamaterials with elegant mechanisms for manipulating the stiffness of the structure in situ covering positive, zero, and negative ranges are highly desired.

Origami provides an elegant means to design metamaterials with tunable properties, such as diverse spatial configurations (*20*–*23*), on-demand deployability (*24*), controllable multistability (*25*), and tunable thermal expansion (*26*) and stiffness (*19*, *20*, *24*, *27*–*29*). However, these strategies for tunable stiffness cannot achieve in situ stiffness manipulation, i.e., the stiffness cannot be altered on demand once the pattern is determined. In addition to the incapability for in situ stiffness manipulation, note that the current origami-based metamaterials are solely based on straight-creased patterns, particularly the so-called rigid origami patterns, in which the deformation energy is theoretically only stored at the creases, not in the origami panels. For example, the well-known Miura pattern and its derivatives have been extensively used (*19*, *20*, *28*, *30*). Although simple, rigid origami patterns have an inherent limitation when used for tunable stiffness, a single energy input from the folding of creases leads to a simple energy landscape and thus a limited range of stiffness tunability. To create a complex energy landscape, another energy input should be considered: energy in the origami panels. Deformable origami falls in this category, although the candidate patterns are very limited (*24*). In addition to in-plane energy in the panel, bending energy in the panel can also be introduced. By combining folding energy at the creases and bending energy in the panel, curved origami can be created (*31*). In contrast to straight creases, there can be multiple curved creases between two points rather than just one straight crease (*32*). The competition between bending energy in the panel and the folding energy at the creases, along with multiple curved creases between two points, would lead to in situ stiffness manipulation covering positive, zero, and negative ranges, which forms the key aspects of this paper.

Here, we designed a family of curved origami–based metamaterials for in situ stiffness manipulation. A specific unit cell of curved origami–based metamaterials was studied, which can be manipulated in situ to exhibit positive, zero, or negative stiffness and functions as a fundamental building block to design curved origami–based metamaterials with different stiffnesses. Then, three applications were presented to demonstrate the unique functions of the metamaterials: a curved origami–based gripper with a negative-stiffness rapid mode or a positive-stiffness precise mode, curved origami cubes for in situ switching between a zero-stiffness vibration isolation mode and a positive-stiffness responsive mode, and a two-dimensional (2D) modular metamaterial for programmable, multistage stiffness responses upon homogenous loading. This work provides an unprecedented principle for curved origami–based mechanical metamaterials for in situ manipulation of stiffness in full ranges, which can be applied in many fields.

## RESULTS

### Rationale of curved origami–based in situ stiffness manipulation

We started by studying two fundamental deformation modes of origami, namely, crease folding and panel bending, with the former for the deformation between creases and the latter for that in the panel.

[1]School for Engineering of Matter, Transport and Energy, Arizona State University, Tempe, AZ 85287, USA. [2]Department of Engineering Mechanics, Zhejiang University, Hangzhou, Zhejiang 310027, China.
*Corresponding author. Email: hanqing.jiang@asu.edu

Figure 1A shows the simplest folding (hereinafter referred to as "folding I") where a horizontal valley crease (marked by a dashed line) is subjected to a compressive load $F$ in the vertical direction. As rigid origami, the only resistance during compression is from the bending at the creases, which provides positive stiffness during the first loading cycle. Upon unloading, the plastic deformation leads to a permanent shape and defines the folded state. The second loading cycle follows the unloading path of the first cycle and the subsequent loading/unloading cycles follow the same route. Another folding mode (hereinafter referred to as "folding II") is when the folding direction is close to the loading direction (Fig. 1B), where a common cell for quadrilateral rigid origami (e.g., Miura pattern), a single-vertex, four-crease pattern with an angle $\beta = 80^\circ$ between a mountain crease (marked by solid line) and valley creases (marked by dashed lines), is subjected to a compressive force $F$ in the vertical direction. Upon compression, this rigid origami exhibits a higher positive stiffness than that shown in Fig. 1A. As shown in the analytical analysis in the Supplementary Materials, for an ideal rigid origami, the initial positive stiffness should be infinite (fig. S1). Then, this positive stiffness quickly transitions to a negative stiffness due to the snap-through at the two vertical valley creases. Theoretical analyses and experimental tests have shown that a positive to negative stiffness transition appears for larger β angles (figs. S1 and S2). Upon unloading, this pattern has plastic deformation, which is also observed in other folding II deformations with different β angles (fig. S1). The second loading cycle follows the unloading path of the first cycle and does not exhibit negative stiffness because the permanent folded state after the first load has exceeded the critical point for the snap-through of the vertical creases. These two types of crease folding describe the key features of rigid origami: positive stiffness from the creases perpendicular to the loading direction and negative stiffness from the creases close to the loading direction due to snap-through, although the negative stiffness may not reappear after the first loading cycle. The third deformation mode is simply a bending mode, which provides positive stiffness and elastic deformation (Fig. 1C). When the vertical straight creases are replaced with a curved crease and the horizontal creases are replaced by the bending mode, curved origami appears. Depending on the curvature of the curved crease, negative stiffness may occur during compression because of the snap-through when the curvature is small (corresponding to a larger β angle for straight creases), whereas the bending mode provides positive stiffness. Connecting two points, there can be multiple curved creases with different curvatures ($\kappa_1$, $\kappa_2$, and $\kappa_3$) and possibly different stiffnesses ($H_1$, $H_2$, and $H_3$) via means such as creases with different thicknesses (Fig. 1D), which would provide a means to switch in situ between different modes for various stiffnesses. This is the rationale to use curved origami for stiffness manipulation.

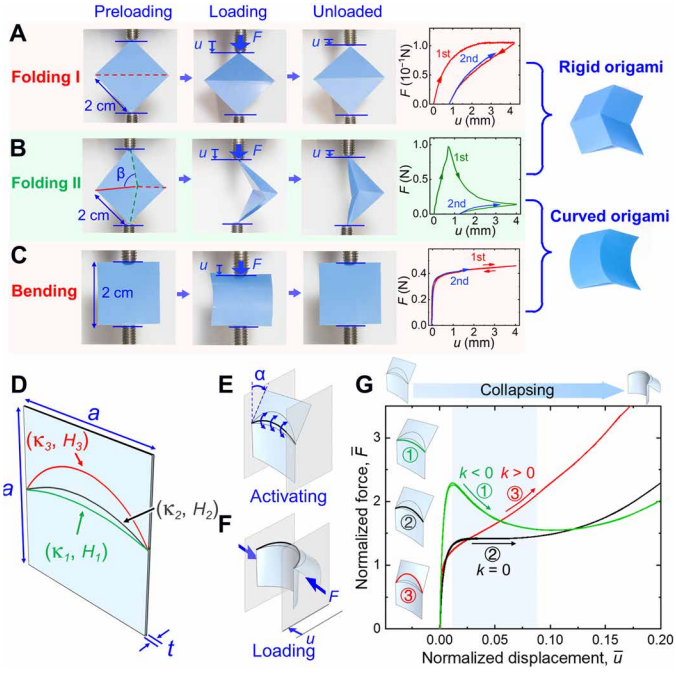


**Fig. 1. Rationale and mechanical behavior of a unit cell of the curved origami.** (**A**) Origami with folding I (a horizontal valley crease in red) under compression and its force-displacement relationship exhibiting positive stiffness. (**B**) Origami with folding II (two valley creases in green close to the loading direction that have an angle $\beta = 80^\circ$ with the mountain crease in red) under compression and exhibiting positive and negative stiffness. The combination of (A) and (B) represent typical deformation modes for rigid origami. (**C**) Plastic film under compression exhibiting bending deformation and positive stiffness. The combination of (B) and (C) represent the deformation modes for curved origami. (**D**) Design of a curved origami unit cell with predefined curved creases ①, ②, and ③, where κ is the curvature and $H$ is the stiffness of the crease. (**E**) Activating a predefined crease of the curved origami unit cell by bending. (**F**) Loading a curved origami unit cell with an activated crease. (**G**) Force-displacement relationship of a unit cell of the curved origami with individually activated curved creases ①, ②, and ③, exhibiting negative, zero, and positive stiffness, respectively. Photo credit: Zirui Zhai, Arizona State University.

Finite element simulations were conducted in ABAQUS to study the stiffness of the square-shaped panel (length $a$, thickness $t$, and elastic modulus $E$) with the coexistence of three arc-shaped creases (curvatures $\kappa_1$, $\kappa_2$, and $\kappa_3$) in the middle (Fig. 1D). The crease modulus $H$ is defined as the applied bending moment per folding angle per crease length and is normalized as $\overline{H} = \frac{Ha}{Et^3}$. The arc-shaped crease can be activated by applying a bending deformation $\alpha = 70^\circ$ (Fig. 1E), and then, a compressive load is applied (Fig. 1F). For a specific crease modulus $\overline{H}_1 = 0.07$, $\overline{H}_2 = 0.03$, and $\overline{H}_3 = 0.01$, the deformed configurations of the curved origami are plotted in fig. S4, and the relationship between the normalized force $\overline{F}$ $(= \frac{Fa}{Et^3})$ and the compressive displacement $\overline{u}$ $(= \frac{u}{a})$ is shown in Fig. 1G. Clearly, the same square with different creases has different stiffness values, which can be positive, zero, or negative, as highlighted in the blue shadowed area. Specifically, crease ① (shown in green) with a smaller curvature $\kappa_1$ exhibits negative stiffness due to the snap-through similar to the folding II mode in Fig. 1B, crease ② (shown in black) with a median curvature $\kappa_2$ exhibits zero stiffness, and crease ③ (shown in red) with a larger curvature $\kappa_3$ exhibits positive stiffness. Hence, hereinafter, we use red, black, and green to represent positive, zero, and negative stiffness, respectively. Thus, the correlation between the curvature and the origami stiffness provides an elegant way to manipulate stiffness.

Figure 2 presents the essential mechanism for using curved origami to provide in situ stiffness manipulation. During the collapse of curved origami, there are two parts of deformation energy: panel bending energy and crease folding energy. For curved origami with only crease ① activated (Fig. 1D), the normalized bending energy in the panel $\overline{U}_b (= \frac{U_b}{Et^3})$, the folding energy at the curved crease $\overline{U}_f (= \frac{U_f}{Et^3})$, and the total energy $\overline{U}_{tot} (= \frac{U_{tot}}{Et^3})$ are plotted for various displacements $\overline{u}$ $(= \frac{u}{a})$

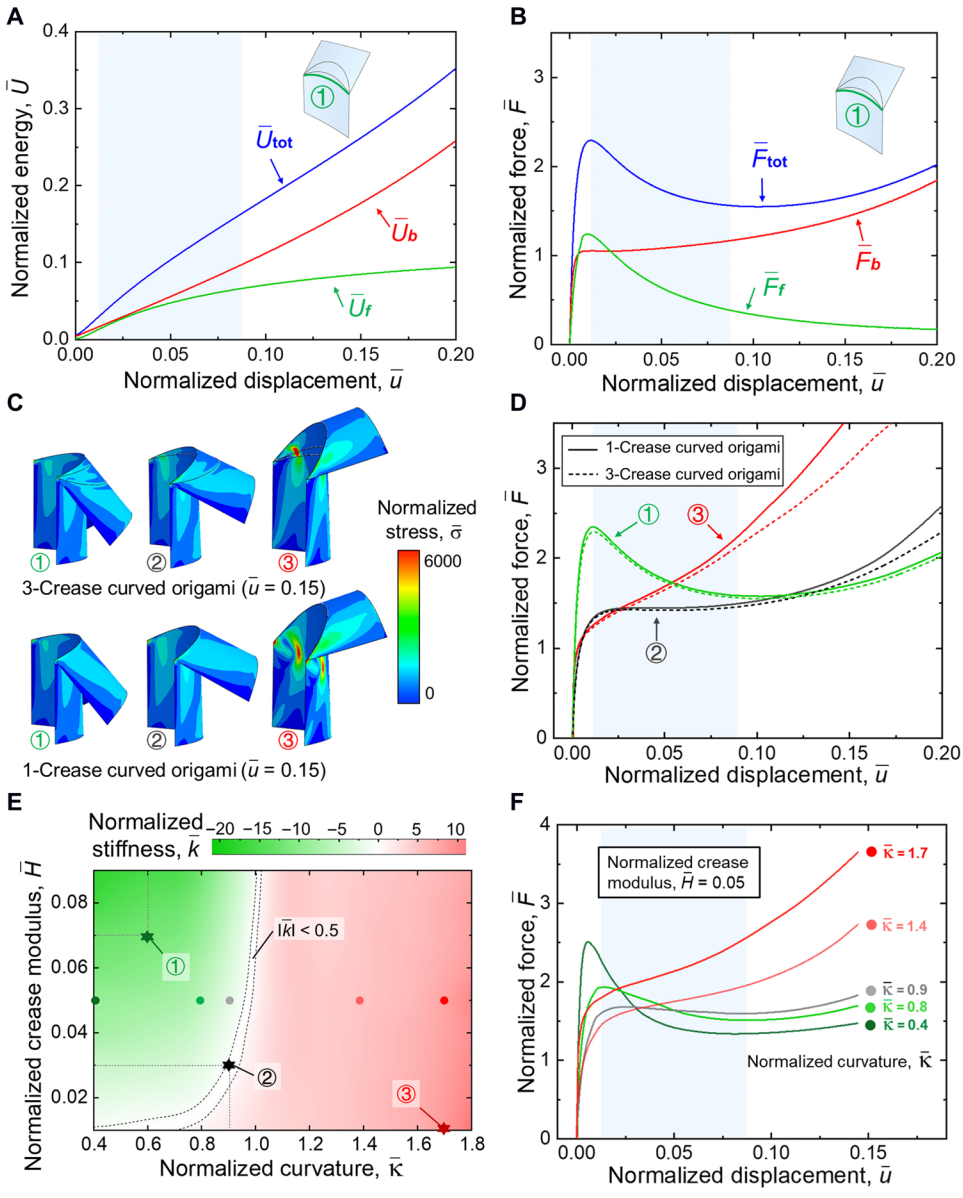


**Fig. 2. Essential mechanism and design guideline of curved origami for in situ stiffness manipulation.** (**A**) Normalized total energy $\bar{U}_{tot}$, bending energy $\bar{U}_b$, and folding energy $\bar{U}_f$ of the curved origami with crease ① activated as a function of normalized displacement $\bar{u}$. (**B**) Normalized total force $\bar{F}_{tot}$, force due to bending $\bar{F}_b$, and force due to folding $\bar{F}_f$ of the curved origami with crease ① activated as a function of normalized displacement $\bar{u}$. (**C**) Comparison of the deformation and stress contour for curved origami with three coexisting creases but only one activated crease and its counterpart with only one curved crease at normalized displacement $\bar{u} = 0.15$. (**D**) Force-displacement relationship of curved origami containing three creases but only one activated crease and its counterpart with only one curved crease. (**E**) Phase diagram of normalized stiffness $\bar{k}$ for single-crease curved origami with a normalized curvature $0.4 < \bar{\kappa} < 2$ and a crease modulus $0.01 < \bar{H} < 0.09$. (**F**) Force-displacement relationship of single-crease curved origami for a given crease modulus $\bar{H} = 0.05$ and varying crease curvatures $\bar{\kappa} = 0.4$, 0.8, 0.9, 1.4, and 1.7.

in Fig. 2A. The total normalized reaction force $\bar{F}_{tot}$ ($= \frac{Fa}{Et^3} = \frac{\partial \bar{U}_{tot}}{\partial \bar{u}}$), which is the derivative of the energy with respect to the displacement, can also be divided into two parts: $\bar{F}_b$ ($= \frac{\partial \bar{U}_b}{\partial \bar{u}}$) due to panel bending and $\bar{F}_f$ ($= \frac{\partial \bar{U}_f}{\partial \bar{u}}$) due to folding at the crease, which are plotted in Fig. 2B for crease ①. The variations in the energies and forces with respect to the displacement for creases ② and ③ are plotted in fig. S5. It is found in all cases that the forces due to panel bending $\bar{F}_b$ and crease folding $\bar{F}_f$ are increasing and decreasing during compression, respectively. Now, it is clear that the bending deformation of the panel provides positive stiffness, whereas the folding at the curved crease provides negative stiffness. By adjusting the contributions of the panel and crease, positive, zero, and negative stiffness can be achieved.

Individual activation of one of multiple coexisting curved creases without (or with negligible) interference is a required characteristic for in situ stiffness manipulation using curved origami. To verify this characteristic, Fig. 2C compares the deformation and stress contour for curved origami with three creases but only one activated crease (Fig. 1D) and its counterpart with only one curved crease at

a given normalized displacement $\bar{u}$ = 0.15. It is clear that these two scenarios are undifferentiable at a given displacement. The relationship between the reaction force $\bar{F}$ and displacement $\bar{u}$ for curved origami with three creases but only one activated crease and its counterpart with just one crease is shown in Fig. 2D, where negligible differences are observed for a given displacement range $0.025 < \bar{u} < 0.075$ for all three curvatures. Moreover, finite element simulations show that only one crease can be activated at a given time, thus ensuring the precise control of creases (section S3 and fig. S6). The negligible interference among the curved creases suggests that the design principle for a single curved crease can be applied to design curved origami with multiple curved creases, providing astounding merit to build a universal phase diagram of a single curved crease through two control parameters: normalized curvature $\bar{\kappa}$ (=$\kappa a$) and crease modulus $\bar{H}$ ($=\frac{Ha}{Et^3}$). Figure 2E provides such a phase diagram for a single crease with a normalized curvature $0.4 < \bar{\kappa} < 1.8$ and a crease modulus $0.01 < \bar{H} < 0.09$. More than 400 cases were simulated through finite element analysis to calculated the stiffness $\bar{k}$ ($=\frac{ka^2}{Et^3}$), and an interpolation was conducted to smooth the plotting. It is observed that by changing the two control parameters $\bar{\kappa}$ and $\bar{H}$, one can readily design curved origami that exhibits a wide spectrum of stiffness $\bar{k}$ ($=\frac{ka^2}{Et^3}$), including positive, zero, and negative values. Given that it is not operationally trivial to change the crease modulus $\bar{H}$ and that it is relatively easy to alter the curvature $\bar{\kappa}$, we presented a relationship between the reaction force $\bar{F}$ and the displacement $\bar{u}$ for a given crease modulus $\bar{H}$ = 0.05 and varying crease curvatures $\bar{\kappa}$ = 0.4, 0.8, 0.9, 1.4, and 1.7 in Fig. 2F, where the dots in dark red to dark green are also shown in Fig. 2E. This figure again shows that in practice, one can achieve positive, zero, and negative stiffness by simply changing the curvature of a crease. A similar plot is shown in fig. S7 for fixed curvature and varied crease moduli. Given the negligible interference among different creases, Fig. 2E essentially provides a design map to create origami with multiple curved creases with any range of stiffness manipulation in two steps: (i) choosing a desired value of stiffness $\bar{k}$ from the stiffness phase diagram and (ii) then locating the corresponding crease curvature and crease modulus. We will demonstrate the in situ stiffness manipulation of curved origami using the following three applications.

## Demonstration I: A lightweight, universal gripper

The first demonstration is a lightweight, universal gripper with two modes: a negative stiffness mode for fast gripping and a positive stiffness mode for precise gripping (Fig. 3). The gripper consists of two plastic films: one handler with an ON/OFF switch for fast and precise gripping and one clipper for gripping objects (Fig. 3A). The ON/OFF switch is realized by activating two curved creases (dashed green lines, $\bar{\kappa}$ = 0.46, and $\bar{H}$ = 0.072; see the Supplementary Materials) with negative stiffness ($k = \frac{\Delta F}{\Delta u} = -0.489$ N/mm at 0.3 mm < $u$ < 2 mm; $k$ = −0.016 N/mm at 3 mm < $u$ < 12 mm) for ON and deactivating the creases for OFF ($k$ = 0.001 N/mm at 0.3 mm < $u$ < 12 mm). The clipper has two curved creases (solid red lines, $\bar{\kappa}$= 1.68, and $H$ = 0.072) and has a positive stiffness ($k$ = 0.109 N/mm at 0.3 mm < $u$ < 12 mm) for actual gripping. The two pieces are connected by tape, as shown in Fig. 3B. The overall stiffness of the gripper can be switched between ON and OFF modes by (de)activating the green curved creases. Top and side views of the gripper in the ON and OFF modes are shown in Fig. 3C. Rubbery pieces were added to increase friction for gripping. To trigger the gripper to switch between ON and OFF modes, one can easily apply bending on the green curved creases to lock the gripper in a desired mode. Movie S1 shows the procedures of switching the gripper between ON and OFF modes. Figure 3D shows the force versus displacement relationship for the ON/OFF modes. Under the same precompression with displacement $u_0$ at point $A$, the ON mode needs a larger preload than the OFF mode, i.e., $F_{ON} > F_{OFF}$. Under displacement-controlled loading, the ON mode has a smaller force increment $\Delta F_{ON}$ to reach the peak force, and then, a snap-through occurs, causing an instantaneous jump to the final state at point $B$ with displacement $u_1$, whereas for the OFF mode, the force gradually increases to the peak with a larger force increment $\Delta F_{OFF}$. It is clear that because of the negative stiffness for the ON mode, high power can be achieved through instantaneously large deformation from $u_0$ = 0.5 mm at the initial state to the final state $u_1$ = 11.6 mm, whereas for the OFF mode, monotonically increased gripping force can achieve precise handling.

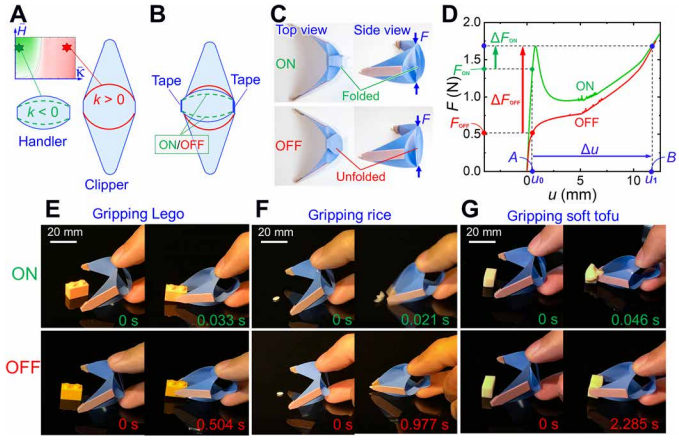


**Fig. 3. Design and testing of a curved origami–based lightweight, universal gripper.** (**A**) Design of the handler part of the gripper with curved creases in green with negative stiffness and the clipper part with curved creases in red with positive stiffness. The inset shows the parameter selections in the stiffness phase diagram. (**B**) The gripper formed with the handler and clipper parts connected by tape and the ON/OFF mode by selecting the appropriate curved creases on the handler part. (**C**) Top and side views of the ON mode (where the creases in green are activated) and OFF mode (where the creases in green are inactivated) of the gripper. (**D**) The force-displacement relationships of the gripper in the ON and OFF modes. Process of gripping (**E**) a Lego block, (**F**) a grain of white rice, and (**G**) a piece of soft tofu, respectively, using both ON and OFF modes of the gripper. The time indicates the time spent gripping the object. Photo credit: Zirui Zhai, Arizona State University.

We conducted experiments to grip different objects with both modes in Fig. 3 (E to G) to demonstrate the importance of switching between ON and OFF modes. For easy-to-grip objects, which are of medium size and regular shape and have a frictional surface, the ON mode will save much time with rapid actuation. In Fig. 3E, when the ON mode is activated, the gripper spent 0.033 s (0.029 s before snap-through and 0.004 s after snap-through) with a speed of 10 m/s (40 mm in 0.004 s), whereas 0.504 s elapsed in the OFF mode. The speed of gripping is higher than the speed of a frog's tongue when capturing prey [1.67 m/s; 50 mm in 0.030 s (*33*)]. Compared with the OFF mode, the ON mode for gripping objects such as a Lego block saves up to 0.471 s (i.e., 93.5% of the time), providing a means for high-efficiency gripping. However, there are also some hard-to-grip objects. Although the ON mode saves time, it may not

be successful or even do harm to the objects. An example is a grain of rice (Fig. 3F), which is small, lightweight, and irregularly shaped. Using the ON mode to grip results in the rice slipping and being kicked away. Using the OFF mode can accurately grip rice without slipping. Another example is soft objects that are likely to be damaged for fast gripping. In Fig. 3G, soft tofu (modulus, 8.005 kPa; strength, 3.298 kPa; and toughness, 875 J/m$^2$) is damaged when gripping with the ON mode, whereas it is safely and effectively gripped with the OFF mode for precise gripping. Movie S2 shows a movie of gripping these three objects. These demonstrations suggest that one can use the same principle to design grippers with more than two modes to realize more selectable modes of different speeds, gripping forces, and actuation responses.

### Demonstration II: A cube with tunable stiffness for controllable force transmissibility

Another demonstration is to use the in situ stiffness manipulation from the curved origami to control force transmissibility. The in situ tunability of force transmissibility is necessary in many situations. For example, people in many areas of the world habitually carry heavy loads on their head instead of by hand or on their shoulders to save energy (*34*, *35*) because the lower stiffness of the neck results in a lower force transmissibility and, thus, a reduced energy cost from the vibrations of loads. Another example is the suspension system in an automobile, which can be switched to a higher stiffness for responsive driving (i.e., sport mode) and a lower stiffness for smooth driving (i.e., comfort mode). Unfortunately, this system is too bulky and complicated to be applied in areas such as robotics. Here, we designed curved origami–based cubes that can switch between an isolating mode and a responsive mode for low-frequency ranges (e.g., lower than 20 Hz). The planar folding pattern is shown in Fig. 4A, in which white, 0.6-mm-thick, plastic panels are used for the top and bottom plates, whereas blue, 0.125-mm-thick, plastic panels are used for the side plates. Tape was used to connect the panels and is represented by thick bars in the folding pattern. The folding creases for modes *A* ($\bar{\kappa} = 1$, $\bar{H} = 0.084$) and *B* ($\bar{\kappa} = 1.8$, $\bar{H} = 0.084$) are represented by black and red lines, respectively, with mode *A* for zero stiffness and mode *B* for positive stiffness, and their locations on the stiffness phase diagram are explicitly shown in the inset of Fig. 4A. The finished cubes at modes *A* and *B* are shown in Fig. 4B. Movie S3 shows the cube and the way to switch between modes *A* and *B*. Figure 4C provides the reaction force-displacement relationship during compression for both modes, which clearly shows that mode *A* exhibits a quasi-zero stiffness and mode *B* exhibits a positive stiffness. Specifically, at a load of 2.35 N, mode *A* exhibits approximately zero stiffness. Hence, 2.35 N is the matching force to achieve quasi-zero stiffness. Near the critical load of 2.35 N, mode *B* exhibits a positive stiffness of $k = 0.584$ N/mm.

We used four curved origami cubes as an array for vibration isolation experiments. Figure 4D shows that the four curved origami cubes of mode *A* can stay balanced at any position when the matching mass of 960 g (equal to 4 × 2.35 N) is applied. A frequency sweep vibration with a power spectrum spreading was used to test the performance of the curved origami isolators. Figure 4E shows the setup of the experiments. An electromechanical shaker (S 51120 from TIRA Vibration Test Systems Inc.) was used to generate vertical vibrations at varied frequencies, and two identical acceleration sensors (352C33 from PCB Piezotronics Inc.) were attached on the bottom and top surfaces to record the input and output accelerations $a_{in}$ and $a_{out}$, respectively. Comparisons of the output and input accelerations of modes *A* and *B* for a frequency sweep vibration are shown in Fig. 4F. The transmissibility of the curved origami isolators in decibels is defined by $20\log_{10}|\frac{a_{out}}{a_{in}}|$. Figure 4G shows the transmissibility at frequencies from 1 to 30 Hz for modes *A* and *B*. The isolators at mode *A* can isolate vibrations (i.e., transmissibility less than 0) when the frequency is higher than 5 Hz. The transmissibility of mode *B* is approximately 20 to 30 dB higher than that of mode *A*, which means that mode *B* can transfer vibration. Movie S4 compares the performances of modes *A* and *B* at fixed frequencies of 10, 12.5, and 15 Hz. Larger output vibrations can be observed at mode *B* for all ranges, suggesting a responsive mode. For mechanical vibrations, the isolation range exists when the vibration frequency is higher than the critical frequency [$f_c = \frac{1}{2\pi}\sqrt{\frac{k}{m}}$ (*36*)]. For mode *A*, the theoretical critical frequency is 0 because the stiffness $k$ is zero, which enables ultralow-frequency vibration isolation. However, because of the plasticity of the creases, the viscoelastic damping of the panels, and the existence of the tape, the isolation is only effective for frequencies higher than 5 Hz. For mode *B*, the theoretical critical frequency is $f_c = \frac{1}{2\pi}\sqrt{\frac{4\times 584\ \text{N/m}}{4\times 240\ \text{g}}} = 7.85$ Hz, which results in the isolation range (frequency higher than 12.5 Hz) of mode *B*. It is believed that this lightweight curved origami–based isolator can be used in many applications in soft and small robotics.

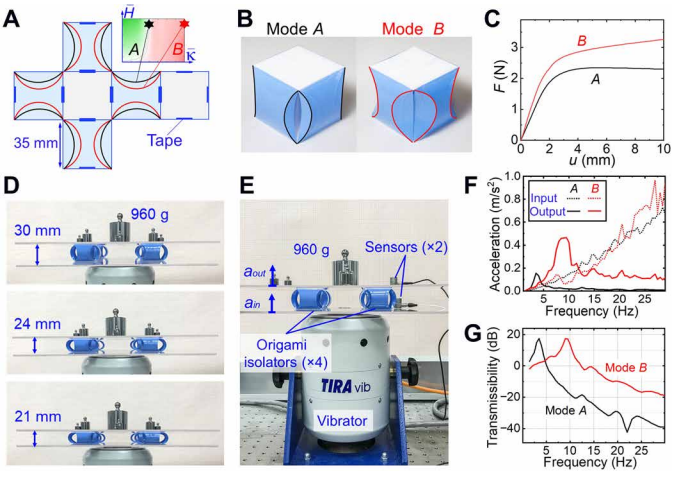


**Fig. 4. Design and experimental characterization of the curved origami cubes for controllable force transmissibility.** (**A**) Design of the curved origami cube with predefined curved creases *A* and *B* and their parameter selections from the stiffness phase diagram. The curved origami cube exhibits negative stiffness when crease *A* is activated, whereas it exhibits positive stiffness when crease *B* is activated. (**B**) Photographs of the curved origami cube in modes *A* and *B*, corresponding to the isolating and responsive modes. Photo credit: Zirui Zhai, Arizona State University. (**C**) Force-displacement relationships of curved origami cubes in modes *A* and *B* exhibiting quasi-zero and positive stiffness, respectively. The required load for quasi-zero stiffness is approximately 2.35 N. (**D**) Photographs showing an array of four curved origami cubes in mode *A* that can stay balanced at any position under its critical load of 960 g (2.35 N). Photo credit: Ken Lin, Zhejiang University. (**E**) Experimental setup used to measure the acceleration transmissibility of the curved origami cubes. Photo credit: Ken Lin, Zhejiang University. (**F**) Input and output accelerations of curved origami cubes in modes *A* and *B* under various vibration frequencies from 1 to 30 Hz. (**G**) Acceleration transmissibility of curved origami cubes in modes *A* and *B* under various vibration frequencies from 1 to 30 Hz.

### Demonstration III: Curved Miura pattern for in situ multistage stiffness response

Here, we design 2D modular metamaterials using curved origami as building blocks, taking a similar approach as the Miura pattern, and demonstrate their unprecedented capability of in situ multistage stiffness response under a uniform load. Figure 5A shows a 3 × 3 Miura pattern, a 3 × 3 curved Miura pattern, and their corresponding unit cells. The curved Miura pattern replaces the mountain creases in the Miura pattern (shown in green) with a curved crease and the two other creases (shown in red) with curved plates. When the top and bottom boundaries are constrained, the curved Miura pattern exhibits different behaviors from the Miura pattern during compression. As shown in movie S5, different deformation modes of curved Miura are observed under different loading conditions (i.e., concentrated loading on the concave side or convex side and uniform loading), and it is found that the deformation can only transfer from the concave side to the convex side. Moreover, when the concave segment is confined, the curved Miura becomes very stiff (fig. S11). Figure 5B shows the deformation of a curved Miura with identical unit cells characterized by the curvature $\bar{\kappa}$ (equal to 0.56) of the crease subjected to a compressive load along the *A*-*A* direction. The concave segment snaps and moves to the right, which is also shown in movie S5. This snap is ubiquitous, as shown in fig. S11, for another crease with curvature $\bar{\kappa}$ = 1.10 that has negative stiffness. For curved Miura patterns that have positive stiffness, snap does not occur, and the applied force monotonically increases with respect to the displacement, which is also shown in fig. S11 for curved origami with curvature $\bar{\kappa}$ = 1.62. Figure 5C compares these three curved Miura patterns with $\bar{\kappa}$ = 0.56 for 1, $\bar{\kappa}$ = 0.95 for 2, and $\bar{\kappa}$ = 1.62 for 3. When 0.125-mm-thick plastic film is used, the normalized crease modulus is $\bar{H}$ = 0.063. On the basis of the stiffness diagram (Fig. 2E), these three curved origami patterns have normalized stiffness $\bar{k}$ = −10.9, −1.6, and 6.1, which leads to snap-through behaviors for 1 and 2 and gradual deformation without snap-through for 3. Upon compressive loading along the *A*-*A* path at progressive displacement *u* = 0, 5, and 10 mm, these three patterns exhibit different responses. Pattern 1 has the highest negative stiffness $\bar{k}$ = −10.9 and the highest transverse displacement of 25 mm, whereas pattern 3 has positive stiffness $\bar{k}$ = 6.1 and the lowest transverse displacement of 9 mm. For the curved Miura with homogeneous curvature, there is a one-to-one relation between the curvature and the transverse displacement under compressive loading, which leads to the design of curved Miura with inhomogeneous curvatures.

Curved Miura with inhomogeneous curvature can be modularly designed to achieve in situ switching and multistage stiffness manipulation. Figure 5D illustrates a 4 × 3 curved Miura with in situ switchable creases along the *A*-*A* and *B*-*B* paths. Along each path, the three creases 1, 2, and 3 that were studied in Fig. 5C can be turned ON or OFF to control the transmissibility of the transverse buckling deformation. As shown in Fig. 5C, transverse buckling always initiates at the concave site of a curved Miura and then propagates inward; thus, this 4 × 3 curved Miura has two transverse buckling paths along Γ and Ξ, and each path has three candidate curvatures 1, 2, and 3. Thus, this 4 × 3 curved Miura can achieve six in situ switchable and accessible states, representing the stiffness response. Considering symmetry, these states can be expressed by a 3 × 3 symmetric matrix shown in Fig. 5E. The switching and compression tests of the six modes are shown in movie S6. Figure 5G

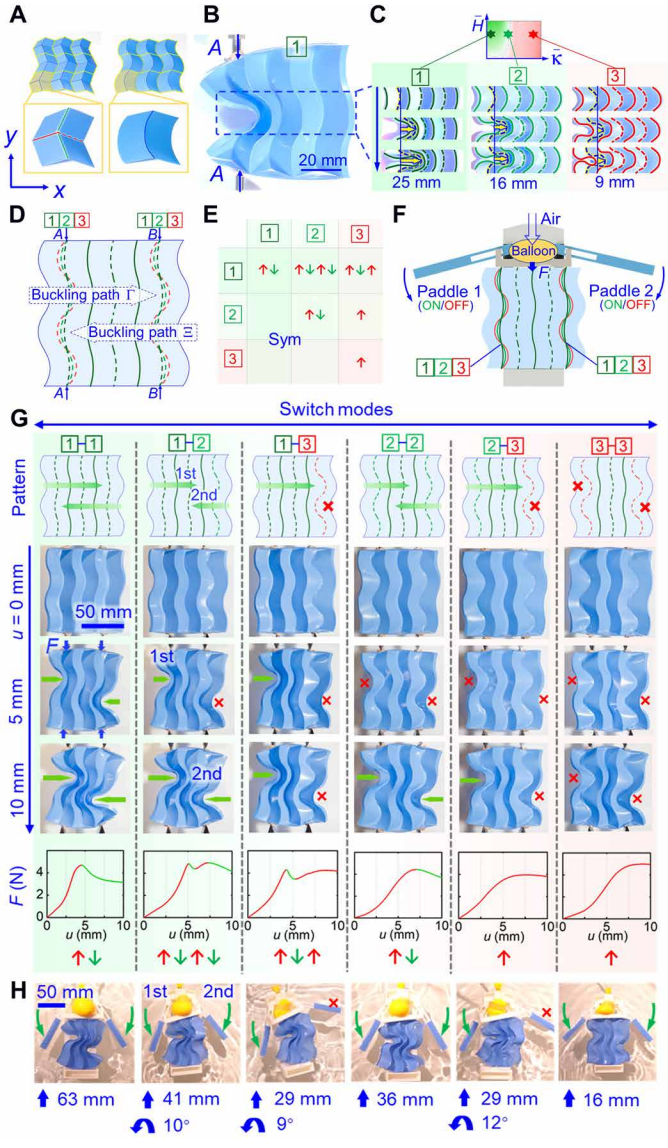


**Fig. 5. Design and performance of the curved Miura pattern and its application in a swimming robot.** (**A**) Photographs of a 3 × 3 Miura pattern and a 3 × 3 curved Miura pattern and their corresponding unit cells. (**B**) A 3 × 3 homogeneous curved Miura with crease 1 ($\bar{\kappa}$ = 0.56) under a compressive load on the *A*-*A* direction. (**C**) The deformation of the middle row of 3 × 3 homogeneous curved Miura with creases 1 ($\bar{\kappa}$ = 0.56), 2 ($\bar{\kappa}$ = 0.95), and 3 ($\bar{\kappa}$ = 1.62) at varied displacements *u* = 0, 5, and 10 mm and the parameter selections of creases 1, 2, and 3 from the stiffness phase diagram. (**D**) Design of a 4 × 3 inhomogeneous curved origami pattern containing three creases 1, 2, and 3 on the leftmost and rightmost boundaries and crease 1 in the middle. (**E**) State matrix of the 4 × 3 inhomogeneous curved Miura representing the force responses of each state, with "↑" denoting increasing force and "↓" denoting decreasing force. (**F**) Design of a pneumatic-driven, curved Miura-based swimming robot. (**G**) Configurations of the six states 1-1, 1-2, 1-3, 2-2, 2-3, and 3-3 and their force-displacement relationship under a uniform compressive load. The green arrow indicates snap-through due to negative stiffness, whereas the red cross indicates no snap-through. (**H**) Photographs of the swimming robot at the six states when the balloon is inflated and the generated linear and rotation displacements of each corresponding state. Photo credit: Zirui Zhai, Arizona State University.

shows the configurations of these six states and their force-displacement responses under a uniform compressive load. Multistage stiffness manipulation is accomplished by a uniform load depending on the ON/OFF combination of different creases. The diagonal components for the matrix in Fig. 5E represent the stiffness response when two identical creases are activated on both paths. When two creases 1 are activated on both paths Γ and Ξ (1-1 combination), the reaction force of this curved Miura will undergo a single peak and then drop because of concurrent transverse buckling at both paths, which is denoted by a ↑↓ stiffness response (with ↑ for peak and ↓ for drop), and a similar situation occurs for a 2-2 combination. When crease 3 is turned ON for both paths, positive stiffness provides a monotonic increase in the force response, which is denoted by ↑. The off-diagonal components in Fig. 5E are for those with nonidentical creases activated. When crease 1 is activated on path Γ and 2 on path Ξ (i.e., a 1-2 combination), the reaction force will experience a peak-valley-peak-valley change, i.e., a ↑ ↓ ↑ ↓ multistage stiffness response achieved by a uniform load. The 1-3 combination exhibits a peak-valley-peak pattern, i.e., ↑ ↓ ↑. The 2-3 combination exhibits a peak-flat pattern, i.e., ↑→. For a curved Miura with more unit cells (e.g., a 6 × 3 pattern), the leftmost and rightmost creases have more choices in terms of curvature (e.g., 4), so a much more complicated stiffness response can be generated, which can be represented by multidimensional tensors. Inhomogeneous curved Miura with in situ switchable curvatures produces complicated multistage stiffness responses under uniform loading. Thus, a controllable and in situ switchable nonlinear mechanism can find many applications, such as in robotics.

One of the challenges in robotics is to accomplish different moving patterns with less actuators to improve the reliability and reduce the cost (*37*). To solve this problem, we built a curved Miura-based swimming robot with a single pneumatic actuator, which can be switched in situ among different actuation modes (Fig. 5F). When air fills the balloon, the inflation compresses the frame in gray that is glued to the curved Miura, and two paddles are attached to the frame via a sliding trench (fig. S12). When the frame moves downwards, the paddle rotates, and the rotation increases as the displacement of the frame increases. On the basis of the matrix in Fig. 5E, the stiffness response with a ↓ mode will lead to a sudden displacement of the frames and thus a larger rotation of the paddle. Consequently, by altering the combinations (e.g., 1-1 and 1-3), six types of complex motions can be realized in situ through simple air flow. Figure 5H and movie S7 show the motion of the robot on water by inflating the balloon using 50 ml of air with a constant flow within 1 s. The activated paddle during motion is highlighted by a green arrow, and the inactivated paddle is indicated by a red cross. The displacement and rotation resulting from the inflation are also presented in Fig. 5H. Modes 1-1, 2-2, and 3-3 have linear displacement without rotation because of the symmetrical buckling in paths Γ and Ξ, with mode 1-1 providing the largest displacement of 63 mm in 1 s because of the largest negative stiffness snap-through, mode 2-2 having a 36-mm displacement because of the snap-through, and mode 3-3 generating the least displacement of 16 mm because of positive stiffness. Modes 1-2, 1-3, and 2-3 provide both linear displacement and rotation because of the asymmetrical deformation of the two paths. The other three modes (i.e., 2-1, 3-1, and 3-2) in Fig. 5E also have asymmetrical motion but clockwise rotation, as shown in movie S8. In summary, the curved Miura-based swimming robot enables different moving modes including fast, slow, linear, and rotational moving with a single pneumatic actuator. This demonstration only presents one of the possible applications to use the in situ multistage stiffness response rooted from curved origami.

## DISCUSSION

In summary, curved origami was introduced here to accomplish in situ stiffness manipulation by changing the curvature of the creases. The variation in stiffness among positive, zero, and negative stiffness results from the competition of the crease folding and the panel bending, with the former providing negative stiffness and the latter providing positive stiffness. The in situ stiffness manipulation is achieved by activating different curved creases on curved origami containing multiple creases. A universal stiffness design diagram was discovered and can be used to design curved creases for specific applications. Three demonstrations were presented to highlight the versatility of the curved origami, including a universal and lightweight gripper, a cube with tunable stiffness for controllable force transmissibility, and curved Miura patterns for in situ multistage stiffness response. This work presents an essential and elegant resolution to use curved origami for complicated, in situ stiffness manipulation, which opens an unexplored direction to design mechanical metamaterials.

Like many other mechanical metamaterials, the presented curved origami needs to be mechanically and manually tuned. A remote-control method will provide better applicability, which can be realized by using temperature-activated (*38*), photoactivated (*39*), electronic (*40*), and magnetic materials (*41*) on the creases. Moreover, the principle of designing curved origami can be extended from the present 1D (e.g., gripper and isolator applications) and 2D (e.g., curved Miura patterns and their application in robots) patterns to 3D and tessellated curved origami scenarios by combining curved origami patterns and other existing designs in origami, e.g., Miura tube design (*20*), multilayered Miura design (*27*), and origami-inspired structural designs (*24*).

We believe that the presented work will establish an essential principle to use various curved origami patterns for designing mechanical metamaterials with unprecedented functions, including stiffness manipulation and deformation reprogramming, which can be readily coupled with other physical fields, such as electromagnetics. Materials and structures created through this principle can be applied in many fields, including daily essentials, protections, robotics, automobiles, aerospace components, and biomedical devices.

## MATERIALS AND METHODS

### Fabrication of curved origami

The curved origami patterns are made of 125-μm-thick (±5 μm) polyester sheets from McMaster-Carr. The outlines and creases of the curved origami are fabricated using a Silhouette Cameo 2 cutter from Silhouette America Inc. The cutting depth of the creases is set to 100 μm for all curved origami.

### Fabrication of the curved origami gripper, curved origami cube, and curved Miura

Heavy-duty packaging tape from the 3M Company is used to connect the polyester plastic film to build curved origami gripper, isolator, and curved Miura. The slow-release foam from

McKeon Products Inc. is used on the curved origami gripper to prevent slippage. The top and bottom panels of the curved origami cubes are fabricated from 635-μm-thick (±64 μm) polyethylene terephthalate glycol plastic films.

### Fabrication of the swimming robot

The frame and the sliding trench of the swimming robot are fabricated using an Ender 3 Pro 3D printer from Shenzhen Creality 3D Technology Co. Ltd. using polylactic acid materials. A 304-mm balloon from Walmart Inc. is used as the actuating balloon in the swimming robots. Clear soft polyvinyl chloride plastic tubes with inner diameters of 0.125 inches and outer diameters of 0.25 inches from McMaster-Carr are used to transfer the air flow. A syringe of 100-ml capacity from McMaster-Carr is used to inflate the balloon.

### Mechanical characterization

An AEL-100-A testing machine from Wenzhou Tripod Instrument Manufacturing Co. Ltd. is used for all the compression and tension tests under a loading speed of 5 mm/min.

### Finite element analysis

ABAQUS (SIMULIA, Providence, RI) commercial software is used to simulate the mechanical behavior of curved origami. Four-node shell elements S4R are used to model the origami panel. Connector elements with one available rotational degree of freedom (DOF) along the crease folding direction and constraints on the other five DOFs are used to model the creases. The panels are modeled as linear elastic materials, and the creases are modeled as linear elastic perfectly plastic materials (with a yield rotation angle of 1 rad).

### Experimental setup for the vibration experiment

The fixed frequency and sweep signals are generated by the signal generation module included in the dynamic signal collection system (LabGenius IM1208H from Inter-Measure Inc.) and then amplified by power amplifiers (BAA 120 from TIRA Vibration Test Systems Inc.). The acceleration signals are measured by two accelerated sensors (352C33 from PCB Piezotronics Inc. and are acquired by the dynamic signal collection system.

## SUPPLEMENTARY MATERIALS

Supplementary material for this article is available at http://advances.sciencemag.org/cgi/content/full/6/47/eabe2000/DC1

## REFERENCES AND NOTES


1. F. P. Beer, E. R. Johnston, J. T. DeWolf, *Mechanics of Materials* (McGraw-Hill Higher Education, 2006).
2. A. Carrella, M. J. Brennan, T. P. Waters, Static analysis of a passive vibration isolator with quasi-zero-stiffness characteristic. *J. Sound Vib.* **301**, 678–689 (2007).
3. B. Haghpanah, L. Salari-Sharif, P. Pourrajab, J. Hopkins, L. Valdevit, Multistable shape-reconfigurable architected materials. *Adv. Mater.* **28**, 7915–7920 (2016).
4. T. Chen, O. R. Bilal, K. Shea, C. Daraio, Harnessing bistability for directional propulsion of soft, untethered robots. *Proc. Natl. Acad. Sci. U.S.A.* **115**, 5698–5702 (2018).
5. J. T. B. Overvelde, T. Kloek, J. J. A. D'haen, K. Bertoldi, Amplifying the response of soft actuators by harnessing snap-through instabilities. *Proc. Natl. Acad. Sci. U.S.A.* **112**, 10863–10868 (2015).
6. C. B. Churchill, D. W. Shahan, S. P. Smith, A. C. Keefe, G. P. McKnight, Dynamically variable negative stiffness structures. *Sci. Adv.* **2**, e1500778 (2016).
7. L. Jin, R. Khajehtourian, J. Mueller, A. Rafsanjani, V. Tournat, K. Bertoldi, D. M. Kochmann, Guided transition waves in multistable mechanical metamaterials. *Proc. Natl. Acad. Sci. U.S.A.* **117**, 2319–2325 (2020).
8. D. P. Ferris, K. Liang, C. T. Farley, Runners adjust leg stiffness for their first step on a new running surface. *J. Biomech.* **32**, 787–794 (1999).
9. M. H. Dickinson, C. T. Farley, R. J. Full, M. A. Koehl, R. Kram, S. Lehman, How animals move: An integrative view. *Science* **288**, 100–106 (2000).
10. R. Sharp, S. Hassan, An evaluation of passive automotive suspension systems with variable stiffness and damping parameters. *Vehicle Syst. Dyn.* **15**, 335–350 (1986).
11. Y. Wei, Y. Chen, T. Ren, Q. Chen, C. Yan, Y. Yang, Y. Li, A novel, variable stiffness robotic gripper based on integrated soft actuating and particle jamming. *Soft Robot.* **3**, 134–143 (2016).
12. I. K. Kuder, A. F. Arrieta, W. E. Raither, P. Ermanni, Variable stiffness material and structural concepts for morphing applications. *Prog. Aerospace Sci.* **63**, 33–55 (2013).
13. H. Pu, S. Yuan, Y. Peng, K. Meng, J. Zhao, R. Xie, Y. Huang, Y. Sun, Y. Yang, S. Xie, J. Luo, X. Chen, Multi-layer electromagnetic spring with tunable negative stiffness for semi-active vibration isolation. *Mechanic. Syst. Sig. Process.* **121**, 942–960 (2019).
14. B. J. Nelson, I. K. Kaliakatsos, J. J. Abbott, Microrobots for minimally invasive medicine. *Annu. Rev. Biomed. Eng.* **12**, 55–85 (2010).
15. S. Kim, C. Laschi, B. Trimmer, Soft robotics: A bioinspired evolution in robotics. *Trends Biotechnol.* **31**, 287–294 (2013).
16. S. Collins, A. Ruina, R. Tedrake, M. Wisse, Efficient bipedal robots based on passive-dynamic walkers. *Science* **307**, 1082–1085 (2005).
17. J. Berger, H. Wadley, R. McMeeking, Mechanical metamaterials at the theoretical limit of isotropic elastic stiffness. *Nature* **543**, 533–537 (2017).
18. S. Janbaz, F. Bobbert, M. Mirzaali, A. Zadpoor, Ultra-programmable buckling-driven soft cellular mechanisms. *Materials Horizons* **6**, 1138–1147 (2019).
19. J. L. Silverberg, A. A. Evans, L. McLeod, R. C. Hayward, T. Hull, C. D. Santangelo, I. Cohen, Using origami design principles to fold reprogrammable mechanical metamaterials. *Science* **345**, 647–650 (2014).
20. E. T. Filipov, T. Tachi, G. H. Paulino, Origami tubes assembled into stiff, yet reconfigurable structures and metamaterials. *Proc. Natl. Acad. Sci. U.S.A.* **112**, 12321–12326 (2015).
21. Z. Yan, F. Zhang, J. Wang, F. Liu, X. Guo, K. Nan, Q. Lin, M. Gao, D. Xiao, Y. Shi, Y. Qiu, H. Luan, J. H. Kim, Y. Wang, H. Luo, M. Han, Y. Huang, Y. Zhang, J. A. Rogers, Controlled mechanical buckling for origami-inspired construction of 3D microstructures in advanced materials. *Adv. Funct. Mater.* **26**, 2629–2639 (2016).
22. Y. Zhang, F. Zhang, Z. Yan, Q. Ma, X. Li, Y. Huang, J. A. Rogers, Printing, folding and assembly methods for forming 3D mesostructures in advanced materials. *Nat. Rev. Mater.* **2**, 17019 (2017).
23. T.-Y. Huang, H. W. Huang, D. D. Jin, Q. Y. Chen, J. Y. Huang, L. Zhang, H. L. Duan, Four-dimensional micro-building blocks. *Sci. Adv.* **6**, eaav8219 (2020).
24. Z. Zhai, Y. Wang, H. Jiang, Origami-inspired, on-demand deployable and collapsible mechanical metamaterials with tunable stiffness. *Proc. Natl. Acad. Sci.* **115**, 2032–2037 (2018).
25. K. Liu, T. Tachi, G. H. Paulino, Invariant and smooth limit of discrete geometry folded from bistable origami leading to multistable metasurfaces. *Nat. Commun.* **10**, 4238 (2019).
26. E. Boatti, N. Vasios, K. Bertoldi, Origami metamaterials for tunable thermal expansion. *Adv. Mater.* **29**, 1700360 (2017).
27. H. Fang, S. C. A. Chu, Y. Xia, K. W. Wang, Programmable self-locking origami mechanical metamaterials. *Adv. Mater.* **30**, 1706311 (2018).
28. J. A. Faber, A. F. Arrieta, A. R. Studart, Bioinspired spring origami. *Science* **359**, 1386–1391 (2018).
29. S. Li, H. Fang, K. Wang, Recoverable and programmable collapse from folding pressurized origami cellular solids. *Phys. Rev. Lett.* **117**, 114301 (2016).
30. C. Lv, D. Krishnaraju, G. Konjevod, H. Yu, H. Jiang, Origami based mechanical metamaterials. *Sci. Rep.* **4**, 5979 (2014).
31. M. A. Dias, L. H. Dudte, L. Mahadevan, C. D. Santangelo, Geometric mechanics of curved crease origami. *Phys. Rev. Lett.* **109**, 114301 (2012).
32. T. U. Lee, Y. Chen, .M. Gattas, *Origami 7: Seventh International Meeting of Origami Science, Mathematics, and Education*, Oxford University, September 4 to 7 2018, vol. 3, pp. 849–864.
33. A. C. Noel, H.-Y. Guo, M. Mandica, D. L. Hu, Frogs use a viscoelastic tongue and non-Newtonian saliva to catch prey. *J. R. Soc. Interface* **14**, 20160764 (2017).
34. G. Maloiy, N. C. Heglund, L. Prager, G. A. Cavagna, C. R. Taylor, Energetic cost of carrying loads: Have African women discovered an economic way? *Nature* **319**, 668–669 (1986).
35. R. M. Alexander, *Elastic Mechanisms in Animal Movement* (Cambridge Univ. Press, 1988), pp. 141.
36. J. P. Den Hartog, *Mechanical Vibrations* (Courier Corporation, 1985).
37. D. Trivedi, C. D. Rahn, W. M. Kier, I. D. Walker, Soft robotics: Biological inspiration, state of the art, and future research. *Appl. Bionics Biomech.* **5**, 99–117 (2008).
38. M. T. Tolley, S. M. Felton, S. Miyashita, D. Aukes, D. Rus, R. J. Wood, Self-folding origami: Shape memory composites activated by uniform heating. *Smart Mater. Struct.* **23**, 094006 (2014).
39. Y. Liu, B. Shaw, M. D. Dickey, J. Genzer, Sequential self-folding of polymer sheets. *Sci. Adv.* **3**, e1602417 (2017).

40. E. Hawkes, B. An, N. M. Benbernou, H. Tanaka, S. Kim, E. D. Demaine, D. Rus, R. J. Wood, Programmable matter by folding. *Proc. Natl. Acad. Sci. U.S.A.* **107**, 12441–12445 (2010).
41. Y. Kim, H. Yuk, R. Zhao, S. A. Chester, X. Zhao, Printing ferromagnetic domains for untethered fast-transforming soft materials. *Nature* **558**, 274–279 (2018).

**Acknowledgments**
**Funding:** H.J. acknowledges support from the NSF under grant no. CMMI-1762792. L.W. acknowledges support from the Guangdong Young Talents Project under grant no. 2018KQNCX269. Y.W. acknowledges support from the National Natural Science Foundation of China under grant nos. 11872328, 11532011, and 11621062 and the Fundamental Research Funds for the Central Universities under grant no. 2018FZA4025. **Author contributions:** Z.Z. and H.J. designed the research. Z.Z., K.L., and L.W. conducted the research and interpreted the results. H.J. supervised the research and interpreted the results. Z.Z., Y.W., and H.J. prepared the manuscript. All authors discussed the results and commented on the manuscript. **Competing interests:** H.J. and Z.Z. are inventors on a provisional patent application related to this work filed on 30 September 2020, no. 63/085,741. The authors declare no other competing interests. **Data and materials availability:** All data needed to evaluate the conclusions in the paper are present in the paper and/or the Supplementary Materials. Additional data related to this paper may be requested from the authors.

Submitted 6 August 2020
Accepted 5 October 2020
Published 18 November 2020
10.1126/sciadv.abe2000

**Citation:** Z. Zhai, Y. Wang, K. Lin, L. Wu, H. Jiang, In situ stiffness manipulation using elegant curved origami. *Sci. Adv.* **6**, eabe2000 (2020).

Science Advances

# In situ stiffness manipulation using elegant curved origami

Zirui Zhai, Yong Wang, Ken Lin, Lingling Wu and Hanqing Jiang

*Sci Adv* **6** (47), eabe2000.
DOI: 10.1126/sciadv.abe2000